ROYAL SOCIETY
OF CHEMISTRY

PAPER

CrossMark
click for updates

Ultrafine nickel–cobalt alloy nanoparticles incorporated into three-dimensional porous graphitic carbon as an electrode material for supercapacitors†

Shengwen Liu,[a] Qian Zhao,[ab] Mingyu Tong,[ab] Xiaoguang Zhu,[a] Guozhong Wang,[a] Weiping Cai,[a] Haimin Zhang*[a] and Huijun Zhao[ac]

Metal oxides are a class of promising electrode materials for supercapacitors because of their high theoretical energy density; however, the low electrical conductivity and instability of metal oxides limit their large-scale practical applications. Here we report a facile and scalable method to synthesize ultrafine nickel–cobalt alloy nanoparticles (5–10 nm) embedded into three-dimensional porous graphitic carbon (3D Ni–Co@PGC) using NaCl as the template to create a porous structure and glucose as the carbon source by pyrolysis treatment at 800 °C under N_2 atmosphere. As an electrode material for supercapacitors, the ultrafine Ni–Co alloy nanoparticles of 3D Ni–Co@PGC not only serve as current collectors, but also their surfaces convert to corresponding metal oxides when exposed to an alkaline electrolyte, responsible for redox reactions in pseudocapacitors, exhibiting high supercapacitor performance. The results demonstrate that the supercapacitor assembled with 3D Ni–Co@PGC electrodes shows high energy density (1091, 1064 and 1041 F g^{-1} at 1, 2 and 4 A g^{-1}, respectively), long cycling life and excellent rate capability at a high charge/discharge current. Furthermore, an asymmetric supercapacitor assembled by using 3D Ni–Co@PGC as the positive electrode and active carbon as the negative electrode shows a high energy density of 33.7 W h kg^{-1} and remarkable cycling stability (98% capacitance retention over 4000 cycles). The superior performance of the 3D Ni–Co@PGC constructed supercapacitor can be ascribed to its high surface area (265 m^2 g^{-1}), porous structure and excellent electrical conductivity, favourable for the exposure of reaction active sites, redox-related mass transport and electron transfer, respectively.

Introduction

Supercapacitors, as electrochemical energy storage and conversion devices, have attracted considerable attention in recent years due to their high power density, long life cycle (>100 000 cycles), and rapid charging and discharging capability, making them the most promising candidates for next generation energy storage devices.[1,2] Generally, the electrode materials for supercapacitors can be classified into two categories on the basis of the energy storage mechanism: electrical

double layer capacitors (EDLCs) and pseudocapacitors.[3] Many capacitive materials have been predicted and developed, such as carbon materials for EDLCs, and RuO_2, MnO_2, TiO_2, NiO, $Ni(OH)_2$ *et al.* for pseudocapacitors.[4] As we know, pseudocapacitors exhibit much larger capacitance values and energy density than EDLCs because the electrode materials possess a variety of reversible oxidation states for highly efficient redox charge transfer.[5,6] Among these electrode materials for pseudocapacitors, nickel and cobalt based oxides/hydroxides should be a class of ideal electrode materials for large-scale applications in supercapacitors due to their remarkable advantages of high theoretical capacitance, low cost and natural abundance.[7–9] Especially, the utilization of Ni, Co composite oxides/hydroxides can synergistically improve the supercapacitors' performance compared to the use of sole Ni or Co based electrode materials, which has been addressed in the reported studies.[10,11] Unfortunately, their practical applications have been hindered because of relatively low electrical conductivity and poor cycle stability, especially at high charge/discharge rates in electrochemical supercapacitors.[12,13] Therefore, it is

[a] Key Laboratory of Materials Physics, Centre for Environmental and Energy Nanomaterials, Anhui Key Laboratory of Nanomaterials and Nanotechnology, Institute of Solid State Physics, Chinese Academy of Sciences, Hefei 230031, China. E-mail: zhanghm@issp.ac.cn

[b] University of Science and Technology of China, Hefei 230026, China

[c] Centre for Clean Environment and Energy, Griffith University, Gold Coast Campus, QLD 4222, Australia

† Electronic supplementary information (ESI) available: Supporting XRD patterns, electron microscopy images and electrochemical test data. See DOI: 10.1039/c6ta06022f

highly desirable for developing low-cost and abundant nickel and cobalt based supercapacitor electrode materials with high energy density, superior electron transfer and mass transport.[14]

To overcome these aforementioned shortcomings, a composite design with conductive reinforcements, such as nanostructured carbon,[15] conducting polymers,[16] nanoporous gold[17] and metal nanoparticles,[18–20] has been employed to enhance the conductivity of pseudocapacitive metal oxide materials. Compositing carbon with pseudocapacitive materials can contribute to a higher capacitance, usually synergistically coming from the high conductivity of carbon and the redox reactions of the pseudocapacitive materials.[21] Some studies have demonstrated that metal oxides encapsulated into porous carbon structures or grown on the conductive substrate can enhance dramatically the performance of capacitors.[22,23] Additionally, metal-oxide/metal composites with enhanced electrical conductivity have been recently developed for maximizing the transition metal oxide potential in supercapacitors.[19,20] It is well reported that three-dimensional (3D) porous carbon nanostructures with large surface area and enhanced electrical conductivity are ideal electrode material supports, favourable for fast ion adsorption/de-adsorption.[18,24,25] Consequently, it should be feasible to incorporate ultrafine metal-oxide/metal nanoparticles into the 3D porous carbon structure to form a high performance electrode material for supercapacitors.

Herein, we report a simple and scalable strategy for the synthesis of ultrafine Ni–Co alloy nanoparticles incorporated in 3D porous graphitic carbon (denoted as 3D Ni–Co@PGC) using NaCl as the porous structure template and glucose as the carbon source by a facile pyrolysis approach. As an electrode material for supercapacitors, 3D Ni–Co@PGC possesses a large surface area of 265 m^2 g^{-1}, porous structure and superior electrical conductivity, thus affording high energy density, long cycling stability and excellent rate capability at a high charge/discharge current. For comparison, Ni–Co alloy nanoparticles embedded into a 3D graphitic carbon structure (denoted as 3D Ni–Co@GC) without the addition of NaCl in the pyrolysis process was also synthesized and measured as the electrode material for supercapacitors.

Experimental

Synthesis of a 3D Ni–Co@PGC composite

In a typical synthesis, 1.0 g $CoCl_2 \cdot 6H_2O$ (Sinopharm Chemical Reagent), 1.0 g $NiCl_2 \cdot 6H_2O$ (Sinopharm Chemical Reagent), 1.0 g NaCl (Sinopharm Chemical Reagent) and 1.0 g glucose (Sinopharm Chemical Reagent) were first dissolved in 15 mL of deionized water. The resultant solution was transferred into a ceramic boat and dried at 60 °C for 10 h in an oven. The obtained mixture was pyrolytically treated at 800 °C for 2 h under an atmosphere of nitrogen. A black powder was obtained and subsequently dispersed into 100 mL of deionized water under stirring for 24 h to completely remove the residual NaCl in the pyrolytic sample. Finally, the black powder product was washed several times with deionized water and centrifuged to collect the 3D Ni–Co@PGC product for further use.

Characterization

Powder X-ray diffraction (XRD) patterns of the samples were recorded on a Philips X-Pert Pro X-ray diffractometer with Cu-Kα radiation (1.5418 Å). Field emission scanning electron microscopy (FESEM) images of the samples were taken on a FESEM (Quanta 200 FEG) operated at an accelerating voltage of 10.0 kV. Transmission electron microscopy (TEM) images of the samples were recorded by a high resolution TEM (JEOL2010), operated at an acceleration voltage of 200 kV. The surface area and porosity of samples were measured by a Surface Area and Porosity Analyzer (Tristar 3020M). Raman spectra of the samples were recorded on a LabRAM HR800 confocal microscope Raman system (Horiba Jobin Yvon) using an Ar ion laser operating at 632 nm.

Electrochemical measurements

For electrochemical measurements, the working electrode was fabricated by mixing active materials, conductive carbon black, and poly(tetrafluoroethylene) (PTFE) at a weight ratio of 8 : 1 : 1, and then the mixture was coated onto a piece of nickel foam with a geometrical area of 1.0 cm^2, and pressed into a thin foil at a pressure of 10.0 MPa. The fabricated electrode was then dried at 60 °C overnight under vacuum conditions. Cyclic voltammetry (CV) and capacitive performance measurements were conducted using a CHI 660D electrochemical workstation (Shanghai Chenhua Instrument, Inc.) in an aqueous KOH electrolyte (6.0 M) with a three-electrode cell. In this setup, the platinum wire served as the counter electrode and an Hg/HgO electrode served as the reference electrode. The mass loading of 3D Ni–Co@PGC on the nickel foam was approximately 2.4 mg cm^{-2}. The specific capacitance was calculated based on the total mass of the active material using the following formula:[7,26]

$$C = I\Delta t/(m\Delta V)$$

where I is the discharge current, Δt is the discharge time, m is the mass of the active material, and ΔV is the voltage window. All the electrochemical measurements were performed at room temperature. Electrochemical impedance spectrometry (EIS) was measured using a CHI 660D electrochemical workstation at a frequency ranging from 100 kHz to 10 mHz.

The asymmetric supercapacitors were fabricated with the 3D Ni–Co@PGC as the positive electrode, active carbon (AC) as the negative electrode, and a porous polymer membrane as the separator. Also, the corresponding AC-based negative electrode was prepared by mixing the AC, carbon black, and PTFE with ethanol at a mass ratio of 80 : 10 : 10. Prior to the fabrication of the asymmetric supercapacitor, the masses of the positive and negative electrodes were balanced according to the following equation:

$$\frac{m_+}{m_-} = \frac{C_-\Delta V_-}{C_+\Delta V_+}$$

where m is the mass, C_s is the specific capacitance, and ΔV is the voltage range for positive (+) and negative (−) electrodes, respectively. Energy density (E) and power density (P) can be calculated as follows:

$$E = 0.5 C_m \Delta V^2$$

$$P = E/\Delta t$$

Results and discussion

Fig. 1 shows the scheme for the preparation of 3D Ni–Co@PGC. The self-stacking of water-soluble NaCl was utilized to form a hard template and $CoCl_2$, $NiCl_2$ crystals were used as nickel–cobalt sources for the formation of 3D Ni–Co@PGC. NaCl, $CoCl_2$, $NiCl_2$ and glucose were first dissolved in deionized water to obtain a homogeneous solution, and then dried at 60 °C for 10 h in an oven. During the drying process, NaCl, $CoCl_2$ and $NiCl_2$ crystals were formed and uniformly coated with a glucose film. After pyrolytic treatment at 800 °C for 2 h in nitrogen atmosphere, the glucose underwent carbonization to form a graphitic carbon structure; meanwhile, ultrafine Ni–Co alloy nanoparticles formed *in situ* onto graphitic carbon because of Ni^{2+} and Co^{2+} at a high pyrolysis temperature, leading to a 3D Ni–Co@GC composite including NaCl crystals (3D Ni–Co/NaCl@GC). After the complete removal of NaCl crystals, 3D porous Ni–Co@GC (3D Ni–Co@PGC) was obtained. Utilization of the NaCl melt salt approach has been reported to fabricate porous graphitic carbon nanosheets for improving their application performance.[27,28] In this work, NaCl was used as the template to create porous structure graphitic carbon incorporated with ultrafine Ni–Co alloy nanoparticles, which would be helpful to facilitate electrochemistry-related mass transport, thus improving the performance of 3D Ni–Co@PGC as an energy storage material.

The XRD spectrum was first recorded to identify the crystal phase of the sample. For comparison, a sample without the addition of NaCl in the synthesis process was also fabricated (denoted as 3D Ni–Co@GC). Fig. 2a shows the XRD patterns of 3D Ni–Co@PGC and 3D Ni–Co@GC. As shown, the peaks around $2\theta = 26.5°$ correspond to the (002) plane of graphitic carbon, confirming the formation of graphitic carbon during the process of glucose carbonization for these two samples.[29] Similarly, the diffraction peaks around 44.34°, 51.66°, and 76.10° for these two samples can be indexed to the (111), (200), and (220) planes of the Ni–Co alloy ($Ni_{50}Co_{50}$ alloy, a fcc structure) with an atomic ratio of 1 : 1;[30,31] their positions are slightly higher than those of pure fcc Co (44.22°, 51.52° and 75.86°, JCPDS card no. 01-1259, Co) and slightly lower than those of pure fcc Ni (44.51°, 51.85° and 76.37°, JCPDS card no. 04-0850,
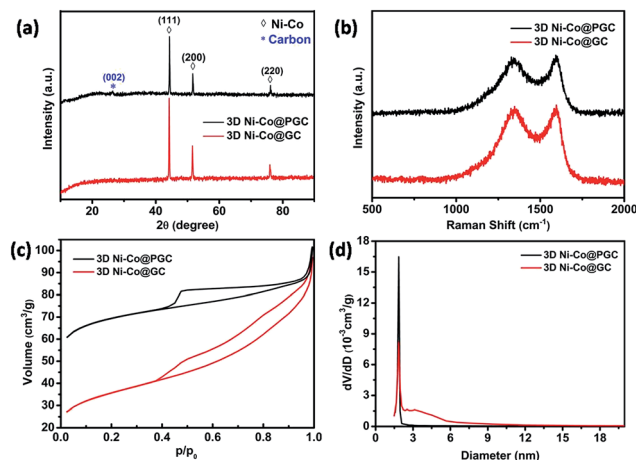

Fig. 2 (a) XRD patterns and (b) Raman spectrum of 3D Ni–Co@GC and 3D Ni–Co@PGC composites, (c) N_2 adsorption–desorption isotherm of 3D Ni–Co@GC and 3D Ni–Co@PGC composites, and (d) their corresponding pore-size distribution curves.

Ni), indicating that glucose derived graphitic carbon can effectively reduce Ni^{2+} and Co^{2+} into a Ni–Co alloy during high temperature pyrolysis. To investigate the influence of NaCl crystals in the composite, the XRD pattern of 3D Ni–Co/NaCl@GC was obtained as shown in Fig. S1 (ESI†). It was found that a NaCl crystal phase (JCPDS: 75-0306) exists in the obtained composite; moreover the introduction of NaCl has no significant influence on the crystal phase of Ni–Co alloy nanoparticles in graphitic carbon. Furthermore, these two samples were also characterized by the Raman spectrum technique (Fig. 2b). The Raman spectra of 3D Ni–Co@GC (black line) and 3D Ni–Co@PGC (red line) display typical Raman peaks of carbon materials at 1350 cm^{-1} of D-band and 1595 cm^{-1} of G-band, corresponding to the vibrations of the carbon atoms with dangling bonds in the plane terminations of disordered graphite and E_{2g} mode of the graphite layer. Generally, the intensity ratio of G band to D band can be used to evaluate the degree of graphitization.[32,33] The I_G/I_D values are 1.01 and 1.02 for 3D Ni–Co@GC and 3D Ni–Co@PGC, respectively, indicating a graphitic carbon structure of all samples, beneficial for improving their electrical conductivity when used as the electrode materials for supercapacitors.

The surface area and pore distribution of 3D Ni–Co@GC and 3D Ni–Co@PGC were measured by N_2 adsorption and desorption isotherms (Fig. 2c). The isotherms of 3D Ni–Co@GC and 3D Ni–Co@PGC display a typical type-IV curve and an H_3-type hysteresis loop, indicating the presence of a porous structure in these two composites. The results demonstrate that 3D Ni–Co@PGC possesses a surface area of 265 m^2 g^{-1} and a pore volume of 0.112 cm^3 g^{-1}, much higher than those of 3D Ni–Co@GC (surface area of 128 m^2 g^{-1} and pore volume of 0.06 cm^3 g^{-1}), mainly attributed to the porous template role of NaCl nanocrystals during high temperature pyrolysis. The pore size distribution calculated using the BJH method by the desorption branch of the nitrogen sorption isotherms shows that 3D Ni–Co@PGC is composed of a porous structure with
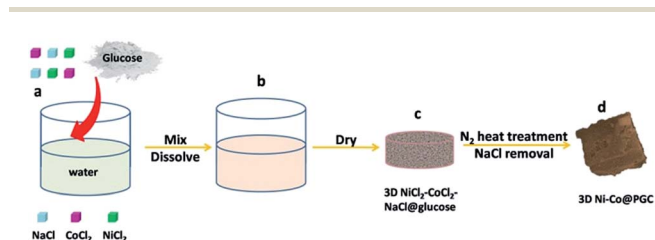

Fig. 1 Schematic illustration of the preparation of a 3D Ni–Co@PGC composite.

17082 | *J. Mater. Chem. A*, 2016, **4**, 17080–17086

This journal is © The Royal Society of Chemistry 2016

a narrow distribution centered at approximately 2.0 nm (Fig. 2d), while the pore sizes are concentrated at 2.0 nm and 3.2 nm for 3D Ni–Co@GC. The above results demonstrate that NaCl crystals as a porous template in high temperature pyrolysis can create a more uniform porous structure. Moreover, it was found that the NaCl amount has significant effects on the surface area and pore volume of the corresponding composites, but their pore size distributions are similar. For example, when more NaCl (*e.g.*, 5.0 g) was used, the fabricated composite (3D Ni–Co@PGC-5) exhibited a higher surface area of 308.5 m^2 g^{-1} and similar pore size distribution with 3D Ni–Co@PGC (Fig. S2, ESI†). The high surface area and porous structure of 3D Ni–Co@PGC are very favourable for the exposure of the reaction active sites and electrochemistry-related mass transfer when used as the electrode material for a supercapacitor, thus improving the device's performance.[34]

The microstructure of 3D Ni–Co@PGC was examined by SEM and TEM techniques. The 3D Ni–Co@PGC mainly consists of cubic-like structures with a rough surface, as shown in Fig. 3a and b, while irregularly shaped bulk structures are obtained for the 3D Ni–Co@GC sample (Fig. S3, ESI†). The above results demonstrate that NaCl crystals may also play an important role in regulating material morphology and structure during high temperature pyrolysis.[27] TEM analysis further indicates that large numbers of nanoparticles are uniformly distributed onto a porous graphitic carbon sheet (Fig. 3c). The sizes of nanoparticles mainly range from 5 to 10 nm, as shown in Fig. 3c and

d. The HRTEM image of 3D Ni–Co@PGC confirms the presence of graphitic carbon layers, and the plane spacing of 0.203 nm and 0.248 nm can be ascribed to the (111) and (110) planes of Ni–Co alloy crystals, as shown in Fig. 3d.[35] Fig. 3e shows the corresponding selected area electronic diffraction (SAED) patterns of 3D Ni–Co@PGC, further indicating the formation of ultrafine Ni–Co alloy crystals on the porous graphitic carbon structure. Fig. 3f shows the EDX mapping images of 3D Ni–Co@PGC, confirming the presence of C, Ni and Co elements and the uniform and overlapped distribution of Ni and Co in the graphitic carbon structure. This also means the formation of ultrafine Ni–Co alloy nanocrystals.

The above characterization results demonstrate that as-prepared 3D Ni–Co@PGC possesses high surface area, porous structure and graphitic carbon structure, possibly favourable for the exposure of reaction active sites provided by Ni–Co related species, electrochemistry-related mass transport and electron transfer when used as the electrode material for supercapacitors. Therefore, the as-prepared 3D Ni–Co@PGC and 3D Ni–Co@GC were used as electrode materials for supercapacitors and evaluated in a 6.0 M KOH solution in this work. Fig. 4a shows the typical CV curves of the 3D Ni–Co@PGC electrode with various sweep rates in the potential window of 0–0.6 V (*vs.* Hg/HgO). It has been generally accepted that the surface of Ni–Co alloy nanoparticles may convert to NiO/Co$_3$O$_4$ and/or Ni(OH)$_2$/Co(OH)$_2$ in an alkaline electrolyte;[36,37] therefore two pairs of redox peaks were observed, corresponding to the reversible reactions of M–O/M–O–OH (M represents Ni or Co).[8] This was also confirmed in this work by XRD and TEM characterizations of the 3D Ni–Co@PGC electrode material after an electrochemical test in a 6.0 M KOH electrolyte. As shown in Fig. S4 (ESI†), the diffraction peaks at 31.3°, 36.9°, 77.5° and 37.2°, 43.2°, 53.7°, 62.9° corresponding to NiO and Co$_3$O$_4$ can be clearly found in the XRD patterns of 3D Ni–Co@PGC after the electrochemical test in a 6.0 M KOH electrolyte. Furthermore,
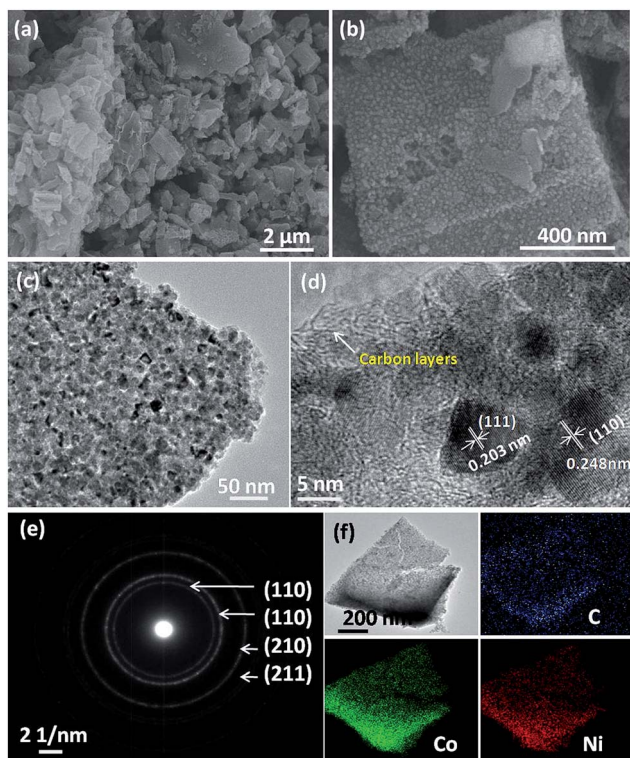

Fig. 3 Microstructure analysis of the 3D Ni–Co@PGC. (a) Low and (b) high magnified SEM images, (c) TEM and (d) HRTEM images, (e) SAED pattern, (f) element distribution in the 3D Ni–Co@PGC and the element mapping results of Co, Ni, and C, respectively.
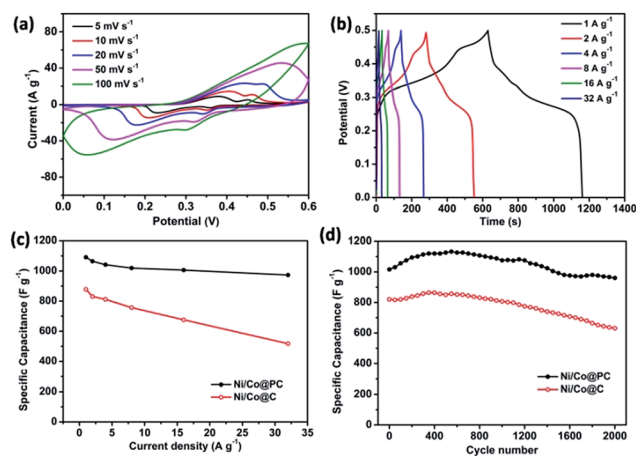

Fig. 4 (a) Cyclic voltammogram curves at various scan rates ranging from 5 mV s^{-1} to 100 mV s^{-1}, (b) charge−discharge curves measured at different current densities of 3D Ni–Co@PGC, (c) average specific capacitance at various current densities and (d) cycling performance at a current density of 2 A g^{-1} of 3D Ni–Co@GC and 3D Ni–Co@PGC.

the HRTEM images (Fig. S5, ESI†) indicate that the lattice spacings of 0.243 nm and 0.209 nm can be indexed to the crystalline planes of (311) of NiO and (202) of Co_3O_4 for 3D Ni–Co@PGC after electrochemical measurements. The above results suggest that NiO and Co_3O_4 derived from the Ni–Co alloy nanoparticles should be responsible for the electrochemical activity of the 3D Ni–Co@PGC electrode material for supercapacitors. As shown in Fig. 4a, with the increase of the scan rate from 5 to 100 mV s^{-1}, the redox peak currents also increase and the shape of the CV curves is well maintained, implying that the 3D Ni–Co@PGC electrode is favourable for ultrafast redox reactions. The slight redox peak shift can be attributed to the polarization effect of the electrode. Fig. 4b shows the galvanostatic charge–discharge curves of 3D Ni–Co@PGC measured at different discharge current densities within the potential window of 0–0.5 V (vs. Hg/HgO). From the correlation of specific capacitances with different current densities, the decrease in capacitances with the increase in current densities may be ascribed to limited ion migration into the interior of the active material.[38] Comparatively, the CV and galvanostatic charge–discharge curves of 3D Ni–Co@GC as plotted in Fig. S6 (ESI†) show that the specific capacitance of the 3D Ni–Co@PGC electrode is much higher than that of the 3D Ni–Co@GC electrode under identical experimental conditions. The specific capacitance as a function of the discharge current density is plotted in Fig. 4c. The 3D Ni–Co@PGC electrode exhibits high specific capacitances of 1091, 1064, 1041, 1019, 1006 and 973 F g^{-1} at the discharge current densities of 1, 2, 4, 8, 16, and 32 A g^{-1}, respectively. Although specific capacitance decreases gradually with increasing current density because of insufficient active materials involved in the redox reaction at high current densities,[39,40] even when the current density is increased to 32 A g^{-1}, the value still remains as high as 973 F g^{-1}, indicating a good rate capability (about 89% of capacitance is retained). These values are much higher than those obtained by 3D Ni–Co@GC and other Ni/Co-based counterparts reported in the literature.[41–43] For 3D Ni–Co@GC, the capacitances are 873, 830, 811, 756, 675 and 517 F g^{-1} at discharge current densities of 1, 2, 4, 8, 16, and 32 A g^{-1}, respectively. The capacitance retention ratio is only 59% when the current density is increased from 1 A g^{-1} to 32 A g^{-1}. Long-term cycling stability has been deemed to be an important parameter of an electrode material for practical application of supercapacitors; therefore the cycling stability of 3D Ni–Co@GC and 3D Ni–Co@PGC electrodes was tested under repeated galvanostatic charge–discharge conditions at a constant current density of 2 A g^{-1} in a 6.0 M KOH electrolyte. As shown in Fig. 4d, the specific capacitance of the 3D Ni–Co@PGC electrode continuously increases until the 1300th cycle, indicating a full activation at the electrode–electrolyte interface in this stage. Compared with the first charge–discharge process, the specific capacitance exhibits no obvious decrease after 1500 cycles (about 95% of capacitance is retained). Whereas, a serious degradation of the specific capacitance of the 3D Ni–Co@GC electrode is observed with only 77% capacitance retention after 2000 cycles. Notably, the porous structure of 3D Ni–Co@PGC with a large surface area can provide sufficient space for electrolyte transport to contact

the reaction active sites provided by the Ni–Co related species during the charge–discharge process, the intimate interaction between the graphitic carbon and ultrafine Ni–Co alloy nanoparticles enables facile electron transport, and the above factors collectively contribute to high specific capacitance, good rate capability and excellent cycle life of the supercapacitor made from the 3D Ni–Co@PGC electrode.[44–46]

To further evaluate the electrochemical properties of the 3D Ni–Co@PGC electrode in supercapacitors, we have constructed an asymmetric supercapacitor (3D Ni–Co@PGC//AC) by employing the 3D Ni–Co@PGC as the positive electrode and the active carbon (AC) as the negative electrode. The detailed electrochemical performance of the AC electrode is presented in Fig. S7 (ESI†); the CV curve of the AC electrode is nearly rectangular shaped with the potential window from −1.0 to 0 V, presenting the characteristics of the double-layer capacitors. The mass ratio of the two electrode materials was balanced before making the asymmetric supercapacitor device, and the voltage window of the asymmetric supercapacitors was determined to be 1.6 V, according to their individual electrochemical behaviours. Fig. 5a shows the CV curves at 5–100 mV s^{-1} which demonstrate that the asymmetric supercapacitor shows an excellent capacitive behaviour at 0–1.6 V. The charge/discharge curves of the asymmetric supercapacitor are shown in Fig. 5b. A high specific capacitance of 107.7 F g^{-1} is reached at 2 A g^{-1} of the asymmetric supercapacitor calculated from the typical galvanostatic charge/discharge curves, and it is 91.7 F g^{-1} with 85% of capacitance retention at 16 A g^{-1}. From the Ragone plot, it is seen that the 3D Ni–Co@PGC//AC asymmetric supercapacitor delivers a high energy density of 33.7 W h kg^{-1} at a power density of 750 W kg^{-1}, and the energy density remains at 28.7 W h kg^{-1} even at a high power density of 6 kW kg^{-1}. These results are much better than those of Ni(OH)$_2$//AC (12.6 W h kg^{-1} at 1.67 kW kg^{-1}),[50] Ni–Co sulfide NWAs//AC (17.8

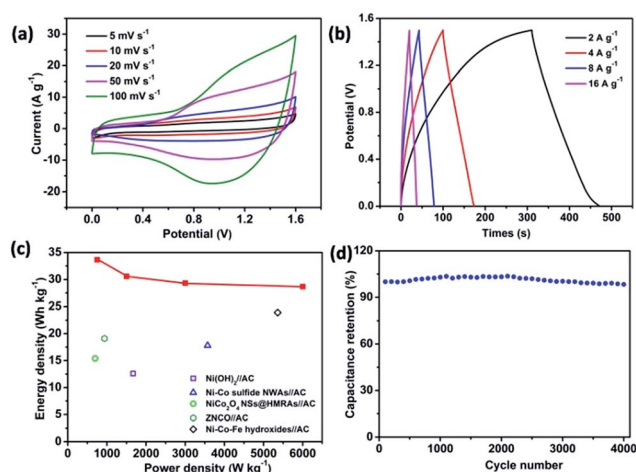Fig. 5 Electrochemical performance of the as-fabricated 3D Ni–Co@PGC//AC asymmetric supercapacitor: (a) CV curves at scan rates of 5–100 mV s^{-1}, (b) galvanostatic charge/discharge curves at different current densities of 2–16 A g^{-1}, (c) the corresponding energy and power densities, and (d) cycling performance at a constant current density of 10 A g^{-1}.
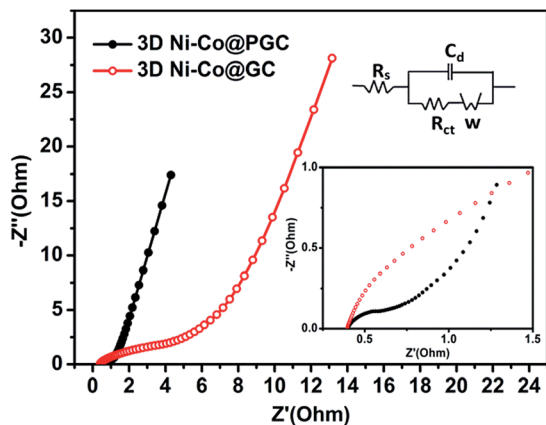
Fig. 6 Nyquist plots of 3D Ni–Co@GC and 3D Ni–Co@PGC electrode materials.

W h kg^{-1} at 3.57 kW kg^{-1}),[51] NiCo$_2$O$_4$ NSs@HMRAs//AC (15.4 W h kg^{-1} at ~0.7 kW kg^{-1}),[52] ZNCO//AC (19.1 W h kg^{-1} at ~0.9 W kg^{-1}),[53] and Ni–Co–Fe hydroxides//AC (23.9 W h kg^{-1} at 5.36 kW kg^{-1}).[54] In addition, the cycling performance of the (3D Ni–Co@PGC//AC) asymmetric supercapacitor is measured at 10 A g^{-1} within the potential window of 0–1.5 V for 4000 cycles, and the curves are displayed in Fig. 5d. The capacitance retention remains at 98% after 4000 cycles. The above results indicate the good stable behaviour of the (3D Ni–Co@PGC//AC) asymmetric supercapacitor.

In general, electrochemical impedance spectroscopy (EIS) was used to investigate the performance of electrochemical capacitors, such as internal resistance, capacity *etc.*[36] The Nyquist plots of 3D Ni–Co@GC and 3D Ni–Co@PGC are shown in Fig. 6, and an equivalent circuit used to fit the Nyquist plots is shown in the inset of Fig. 6. At high frequency, the intercept on the real axis represents a combined resistance (R_s) resulting from the resistance of the electrode materials, the ionic resistance of the electrolyte and the active material/current collector interface.[39,51] The R_s values for 3D Ni–Co@GC and 3D Ni–Co@PGC electrodes were measured to be 0.42 Ω and 0.41 Ω, respectively. Clearly, the good electrical conductivity of 3D Ni–Co@GC and 3D Ni–Co@PGC electrodes is evident from their similar and low R_s values. The semicircle in the high-frequency range corresponds to the charge transfer resistance (R_{ct}) caused by faradic reactions.[47–49] The fitted values of R_{ct} are about 0.48 Ω and 0.13 Ω for 3D Ni–Co@GC and 3D Ni–Co@PGC electrodes, respectively. An electrode with a lower R_{ct} value is more effective for fast charge and discharge responses. The reduced charge-transfer resistance for the 3D Ni–Co@PGC electrode can be attributed to its high surface area and uniformly distributed ultrafine Ni–Co alloy nanoparticles providing more reaction active sites, indicating high electrochemical reaction activity as an electrode material for supercapacitors.

Conclusion

In summary, we reported a facile and scalable method to *in situ* prepare ultrafine Ni–Co alloy nanoparticles incorporated into a 3D porous graphitic carbon composite using NaCl as the porous template and glucose as the carbon source by a simple pyrolysis approach. Owing to its high surface area, porous structure and superior electrical conductivity, the prepared 3D Ni–Co@PGC as the electrode material for a supercapacitor exhibited excellent performance of the supercapacitor with large specific capacitance, high rate capability and good cycling stability. The synthesis strategy used in this work can be extended to fabricate other transition metal alloy nanoparticle incorporated porous graphitic carbon composites for energy storage applications.

Notes and references

1 P. Simon and Y. Gogotsi, *Nat. Mater.*, 2008, **7**, 845–854.
2 L. L. Zhang and X. Zhao, *Chem. Soc. Rev.*, 2009, **38**, 2520–2531.
3 G. Wang, L. Zhang and J. Zhang, *Chem. Soc. Rev.*, 2012, **41**, 797–828.
4 L. Feng, Y. Zhu, H. Ding and C. Ni, *J. Power Sources*, 2014, **267**, 430–444.
5 H. B. Li, M. H. Yu, F. X. Wang, P. Liu, Y. Liang, J. Xiao, C. X. Wang, Y. X. Tong and G. W. Yang, *Nat. Commun.*, 2013, **4**, 1894.
6 V. Augustyn, P. Simon and B. Dunn, *Energy Environ. Sci.*, 2014, **7**, 1597–1614.
7 M. Jana, S. Saha, P. Samanta, N. C. Murmu, N. H. Kim, T. Kuila and J. H. Lee, *J. Mater. Chem. A*, 2016, **4**, 2188–2197.
8 D. Li, Y. Gong, Y. Zhang, C. Luo, W. Li, Q. Fu and C. Pan, *Sci. Rep.*, 2015, **5**, 12903.
9 M. Rui, X. Li, L. Gan, T. Zhai and H. Zeng, *Adv. Funct. Mater.*, 2016, **26**, 5051.
10 L. Yu, B. Guan, W. Xiao and X. W. Lou, *Adv. Energy Mater.*, 2015, **5**, 1500981.
11 L. Huang, D. Chen, Y. Ding, S. Feng, Z. L. Wang and M. Liu, *Nano Lett.*, 2013, **13**, 3135–3139.
12 S. J. Peng, L. L. Li, H. B. Wu, S. Madhavi and X. W. Lou, *Adv. Energy Mater.*, 2015, **5**, 1401172.
13 F. Zhou, Q. Liu, J. Gu, W. Zhang and D. Zhang, *J. Power Sources*, 2015, **273**, 945–953.
14 Y. Xu, Y. Tao, X. Zheng, H. Ma, J. Luo, F. Kang and Q. H. Yang, *Adv. Mater.*, 2015, **27**, 8082–8087.
15 M. Zhi, C. Xiang, J. Li, M. Li and N. Wu, *Nanoscale*, 2013, **5**, 72–88.
16 T. Qian, N. Xu, J. Zhou, T. Yang, X. Liu, X. Shen, J. Liang and C. Yan, *J. Mater. Chem. A*, 2015, **3**, 488–493.

17 X. Lang, A. Hirata, T. Fujita and M. Chen, *Nat. Nanotechnol.*, 2011, **6**, 232–236.

18 Y. Gao, L. Wang, W. Zhang, X. Yang, Y. Ma, J. Shao and Y. Li, *Electrochim. Acta*, 2016, **201**, 260–267.

19 H. Lai, Q. Wu, J. Zhao, L. Shang, H. Li, R. Che, Z. Lyu, J. Xiong, L. Yang, X. Wang and Z. Hu, *Energy Environ. Sci.*, 2016, **9**, 2053–2060.

20 X. H. Xia, Y. Q. Zhang, Z. X. Fan, D. L. Chao, Q. Q. Xiong, J. P. Tu, H. Zhang and H. J. Fan, *Adv. Energy Mater.*, 2015, **5**, 1401709.

21 H. Jiang, J. Ma and C. Li, *Adv. Mater.*, 2012, **24**, 4197–4202.

22 G. Q. Zhang, H. B. Wu, H. E. Hoster, M. B. Chan-Park and X. W. Lou, *Energy Environ. Sci.*, 2012, **5**, 9453–9456.

23 R. R. Salunkhe, J. Tang, Y. Kamachi, T. Nakato, J. H. Kim and Y. Yamauchi, *ACS Nano*, 2015, **9**, 6288–6296.

24 H. Jiang, P. S. Lee and C. Li, *Energy Environ. Sci.*, 2013, **6**, 41–53.

25 D. W. Wang, F. Li, M. Liu, G. Q. Lu and H. M. Cheng, *Angew. Chem., Int. Ed.*, 2008, **47**, 373–376.

26 S. Chen, J. Zhu, X. Wu, Q. Han and X. Wang, *ACS Nano*, 2010, **4**, 2822–2830.

27 G. Li, J. Sun, W. Hou, S. Jiang, Y. Huang and J. Geng, *Nat. Commun.*, 2016, **7**, 10601.

28 M. Al-Mamun, X. Su, H. Zhang, H. Yin, P. Liu, H. Yang, D. Wang, Z. Tang, Y. Wang and H. Zhao, *Small*, 2016, **12**, 2866–2871.

29 S. Liu, H. Zhang, Q. Zhao, X. Zhang, R. Liu, X. Ge, G. Wang, H. Zhao and W. Cai, *Carbon*, 2016, **106**, 74–83.

30 Y. Li, L. Li, H. Liao and H. Wang, *J. Mater. Chem.*, 1999, **9**, 2675–2677.

31 C. Jiao, L. Sun, F. Xu, S. S. Liu, J. Zhang, X. Jiang and L. Yang, *Sci. Rep.*, 2016, **6**, 27429.

32 P. Zhang, F. Sun, Z. H. Xiang, Z. G. Shen, J. Yun and D. P. Cao, *Energy Environ. Sci.*, 2014, **7**, 442–450.

33 S. Liu, X. Wang, H. Zhao and W. Cai, *Colloids Surf., A*, 2015, **484**, 386–393.

34 T. Y. Wei, C. H. Chen, H. C. Chien, S. Y. Lu and C. C. Hu, *Adv. Mater.*, 2010, **22**, 347–351.

35 S. Zhou, M. Wen, N. Wang, Q. Wu, Q. Wu and L. Cheng, *J. Mater. Chem.*, 2012, **22**, 16858–16864.

36 M.-S. Wu and W.-H. Hsu, *J. Power Sources*, 2015, **274**, 1055–1062.

37 N. H. Chou, P. N. Ross, A. T. Bell and T. D. Tilley, *ChemSusChem*, 2011, **4**, 1566–1569.

38 R. Wu, D. P. Wang, V. Kumar, K. Zhou, A. W. K. Law, P. S. Lee, J. Lou and Z. Chen, *Chem. Commun.*, 2015, **51**, 3109–3112.

39 H. Wan, J. Jiang, J. Yu, K. Xu, L. Miao, L. Zhang, H. Chen and Y. Ruan, *CrystEngComm*, 2013, **15**, 7649–7651.

40 X. Xiong, D. Ding, D. Chen, G. Waller, Y. Bu, Z. Wang and M. Liu, *Nano Energy*, 2015, **11**, 154–161.

41 F. Cai, Y. Kang, H. Chen, M. Chen and Q. Li, *J. Mater. Chem. A*, 2014, **2**, 11509–11515.

42 G. Gao, H. B. Wu, S. Ding, L.-M. Liu and X. W. Lou, *Small*, 2015, **11**, 804–808.

43 X. Liu, S. Shi, Q. Xiong, L. Li, Y. Zhang, H. Tang, C. Gu, X. Wang and J. Tu, *ACS Appl. Mater. Interfaces*, 2013, **5**, 8790–8795.

44 W. Fu, C. Zhao, W. Han, Y. Liu, H. Zhao, Y. Ma and E. Xie, *J. Mater. Chem. A*, 2015, **3**, 10492–10497.

45 Y. Shao, M. F. El-Kady, C. W. Lin, G. Zhu, K. L. Marsh, J. Y. Hwang, Q. Zhang, Y. Li, H. Wang and R. B. Kaner, *Adv. Mater.*, 2016, **28**, 6719.

46 L. Mao, C. Guan, X. Huang, Q. Ke, Y. Zhang and J. Wang, *Electrochim. Acta*, 2016, **196**, 653–660.

47 G. Nagaraju, R. Kakarla, S. M. Cha and J. S. Yu, *Nano Res.*, 2015, **8**, 3749–3763.

48 Q. Wang, L. Jiao, H. Du, Y. Si, Y. Wang and H. Yuan, *J. Mater. Chem.*, 2012, **22**, 21387–21391.

49 Z. Huang, Z. Zhang, X. Qi, X. Ren, G. Xu, P. Wan, X. Sun and H. Zhang, *Nanoscale*, 2016, **8**, 13273–13279.

50 H. Li, M. Yu, F. Wang, P. Liu, Y. Liang, J. Xiao, C. Wang, Y. Tong and G. Yang, *Nat. Commun.*, 2013, **4**, 1894.

51 Y. Li, L. Cao, L. Qiao, M. Zhou, Y. Yang, P. Xiao and Y. Zhang, *J. Mater. Chem. A*, 2014, **2**, 6540–6548.

52 X.-F. Lu, D.-J. Wu, R.-Z. Li, Q. Li, S.-H. Ye, Y.-X. Tong and G.-R. Li, *J. Mater. Chem. A*, 2014, **2**, 4706–4713.

53 C. Wu, J. Cai, Q. Zhang, X. Zhou, Y. Zhu, P. K. Shen and K. Zhang, *ACS Appl. Mater. Interfaces*, 2015, **7**, 26512–26521.

54 H. Li, Y. Gao, C. Wang and G. Yang, *Adv. Energy Mater.*, 2015, **5**, 1401767.